Cao, C., Hill, T. L., Li, B., Wang, L., & Gao, X. (2020). Nonlinear dynamics of a conical dielectric elastomer oscillator with switchable mono to bi-stability. *International Journal of Solids and Structures*. https://doi.org/10.1016/j.ijsolstr.2020.02.012

# Nonlinear dynamics of a conical dielectric elastomer oscillator with switchable mono to bi-stability

Chongjing Cao [1], Thomas L. Hill [2], Bo Li [3], Lei Wang [1], Xing Gao [1*]

[1] Research Centre for Medical Robotics and Minimally Invasive Surgical Devices, Shenzhen Institutes of Advanced Technology (SIAT), Chinese Academy of Sciences, Shenzhen 518055, China
[2] Department of Mechanical Engineering, University of Bristol, Bristol BS8 1TR, UK
[3] Shaanxi Key Lab of Intelligent Robots, School of Mechanical Engineering, Xi'an Jiaotong University, Xi'an 710049, China
* Corresponding address: xing.gao@siat.ac.cn

## Abstract

Dielectric elastomer actuators (DEAs) are an emerging type of soft actuator that show many advantages including large actuation strains, high energy density and high theoretical efficiency. Due to the inherent elasticity, such actuators can also be used as soft oscillators and, when at resonance, the dielectric elastomer oscillators (DEOs) can exhibit a peak oscillation amplitude and power output with an improved energy efficiency in comparison to non-resonant behaviour. However, most existing DEOs have a fixed pre-defined morphology and demonstrate a single stable equilibrium, which limits their versatility. In this work, a conical DEO is proposed which may exhibit either monostability (i.e. one stable equilibrium point) or bistability (two equilibria). The system demonstrates a transition between two regimes using a voltage control. Such a feature allows the DEO system to have multiple oscillation modes with different equilibrium points and the transition between equilibria is controlled by an effective control strategy proposed in this work. A mathematical model based on the Euler-Lagrange method is developed to investigate the stability of this system and its complex nonlinear dynamic response in unforced and parametrically forced cases. This design has potential in more advanced and versatile DEO applications such as active vibrational controllers/ shakers, active morphing structures, smart energy harvesting and highly programmable robotic locomotion.

**Key words**: Dielectric Elastomer Oscillators; Nonlinear Dynamics; Programmable Oscillation; Active Morphing Structure; Stability Control; Rigid-compliant Interaction

## 1. Introduction

Dielectric elastomer actuators (DEAs) are one type of electro-active polymer that show advantages over conventional actuators in terms of large actuation strain, high theoretical efficiency, inherent compliance and low cost [1]. An idealized DEA consists of a piece of dielectric elastomer sandwiched between two compliant electrodes. When a voltage is applied across the electrodes, the electric field generates electrostatic pressure that causes the membrane to contract in thickness and expand in area. Many configurations of DEAs have been proposed, such as the stacked DEAs [2] [3] [4], conical DEAs [5] [6] [7], rolled DEAs [8] [9] [10] and the DE minimum energy structures

(DEMES) [11] [12] [13] [14].

Due to the inherent elasticity, when stimulated by an alternating current (AC) voltage signal, the DEAs can generate oscillatory motions, which can be termed as DE oscillators (DEOs). As the excitation frequency approaches the natural frequency of the DEO system, it can exhibit a dramatic increase in its oscillation amplitude. This soft oscillation technology can have advantages over other conventional rigid mechanical oscillators in terms of inherent compliance, which can be readily integrated with soft robotic systems to allow safer human-robot interaction, morphological computation and other advanced applications [15].

Several studies have investigated the dynamic response of DEOs with different configurations either theoretically or experimentally (see, e.g. [16] [17] [18] [19] [20] [21] [22] [23] [24] [25] [26] [27] [28] [29] [30] [31]). One of the earliest works on the dynamics of DEOs was conducted by Fox & Goulbourne, (2008 & 2009), in their works, the dynamics of a DE balloon was investigated with different resonant modes of the membrane captured [16] [17]. This configuration was then investigated further using a thermodynamics framework [18] [19]. Based on this framework, many other configurations of DEOs have also been studied. For example, Zhang *et al*. conducted a series of works on the idealized rectangular DEOs in which the strong coupling of the oscillation response in the two in-plane directions was exposed [20] and the geometrical effects on its dynamics were investigated [21]. Pure-shear DEOs were studied extensively with the focus on the effects of biasing elements [23], strain-stiffing in the DE membranes [24], the viscosity-induced drifting in the equilibrium states [25] and the safe actuation voltage ranges [22]. Zhao *et al*. [32] and Wang *et al*. [33] have demonstrated experimentally that, by applying a voltage impulse, a bistable DEMES can transit between two stable states. Many dynamic applications based on DEOs have been developed in soft robotic locomotion [27] [34] [35] [36] [37] [38] [39], a pneumatic pump [40], grippers [33] [41], a loudspeaker [42], noise cancellation [43] [44] and vibrational control [45] [46].

It is worth noting that, most previous DEO designs incorporate only the compliant DE membranes as the mean of generating oscillatory motions and have a fixed pre-defined morphology. These designs are restricted to a predetermined number of stable equilibrium states (either one or two equilibria), which, to some extent limits their versatility. For instance, in soft vibrational locomotion applications, DEOs are commonly adopted as the vibrational source. However, due the fixed stability of the DEOs, such vibrational robots can only move in one direction if no additional steering control system is added [38]. A DEO design that has multiple stable states could potentially reduce such design complexity, in robotic systems, by taking advantage of its multiple oscillation modes (oscillations around different equilibria with various amplitudes) as means for steering / velocity controls [27]. To the best of the authors' knowledge, no work has focused on the development of a DEO configuration with multiple controllable stable states, nor has investigated the nonlinear dynamic behaviour they may exhibit.

In this paper, we propose a novel DEO system that incorporates a rigid-compliant interaction between the biasing mechanism and the DE membrane. The rigid-compliant interaction allows this DEO design to switch between *monostable* (i.e. one stable equilibrium point) and *bistable* (two equilibria) modes by active voltage control and design parameter tuning. The bistablility

demonstrated by this design allows a rapid yet safe switch between two stable states. In comparison, conventional bistable DEA systems commonly adopt a *snap-through* mechanism induced by the electro-mechanical instability, which can have the potential risk of electric breakdown and unpredictable responses [47] [48]. The controllability of this novel DEO design also allows a programmable oscillation mode around the targeted equilibrium, which can potentially lead to more advanced and versatile DEO applications such as active vibrational control, active morphing structures, smart energy harvesting and highly programmable robotic locomotion. A mathematical model is also developed in this work to investigate the stability of this system and its complex nonlinear dynamic response.

The rest of this paper is structured as follows. In Section 2, the oscillator configuration and working principle is introduced. In Section 3, a theoretical model is derived using the Euler-Lagrange method. Based on this model, its static equilibrium states and small perturbations around these equilibrium states are investigated in Section 4. In Section 5, the free oscillation as a conservative system and the effects of damping and static biasing voltage are analysed systematically. Section 6 focuses on the parametric excitation of this DEO system and Section 7 presents an effective control strategy for the bistable mode DEO that allows a robust transition between the two equilibria. Finally, conclusions are drawn in Section 8 and potential applications of this system are discussed.

## 2. DEO design and working principle

This section describes the design concept of the proposed DEO and its fundamental working principle. The DEO structure consists of a circular DEA coupled with a bistable spring mechanism, as illustrated in **Figure 1** (**a**), where $F_s$ is the spring force and $F_{DEA}$ is the tensile force of DEA in the $x$ axis. The circular DEA shares the same design as in previous works [5] [6] [30] [31] [49] [50] [51] [52] [53], where a pre-stretched DE membrane is bonded to a rigid circular frame with a disk attached to the centre. The biasing mechanism consists of two linear springs with the distance between the fixed ends smaller than the total length of the two springs. In this design, the motion of the DEA and the biasing mechanism is restricted to one degree-of-freedom (DOF) horizontal translation. The curve on the right of each component in **Figure 1** (**a**) shows the force-displacement function along the horizontal axis. This bistable biasing mechanism differs from the previous bistable buckling beam mechanisms used in DEAs [54] [55] [56] [57] [58] as it allows a continuum deformation post bucking of the springs. This opens the potential for high amplitude oscillations that cannot be achieved in previous bistable DEA designs. The DEO system can exhibit three possible static equilibrium states, in which two are stable (Equilibria (i) and (ii)) and one is unstable (Equilibrium (iii)), as illustrated in **Figure 1** (**b**). However, it is worth noting that, depending on the specific parameter values, monostability can also exist in this system, i.e. Equilibrium (iii) in **Figure 1 (b**) becomes the only stable solution. Detailed study of the static equilibrium states is conducted in Section 3.

The quasi-static actuation principle of this system can be explained by the force balance between the tension-induced force of the DE membrane and the restoring force of the bistable mechanism. When in passive equilibrium (no applied voltage), the tension of the membrane is balanced by the compressed springs in the horizontal axis. As a voltage is applied across the DE membrane, the electrostatic pressure, induced by the electric field, reduces the tension on the membrane, which

results in a force imbalance. The membrane is then deformed out-of-plane further until another force equilibrium state is achieved, as illustrated in **Figure 1** (**c**). When the voltage is removed, the membrane will return to its passive equilibrium. If an AC voltage is applied instead of a direct current (DC) voltage, the DEO will oscillate around its equilibrium point and the amplitude of this oscillation is a function of the voltage amplitude and frequency.

## 3. Mathematical modelling

In this section, a numerical model is developed to characterize the responses of the DEO system. The following assumptions are made in this model, following [5] [31] [49] [53] [59] [60]. (i) This is a single DOF system, i.e. this model restricts itself in a translation along the horizontal axis; (ii) force due to gravity is neglected; (iii) the out-of-plane deformation is approximated as being conical; (iv) the strain distribution on the membrane is homogenous; (v) the circumferential deformation of the membrane does not vary.

In its resting state, the DE membrane has an initial thickness of $H_0$. It is first pre-stretched in biaxial directions by a ratio of $\lambda_p$ and then bonded to a central disk, with the outer radius $a$, and a rigid ring, with the inner radius $b$. When coupled with the biasing mechanism, the membrane is deformed out-of-plane, by a distance $d_0$. The horizontal deformation of the biasing mechanism (i.e. the distance between the free moving end and the fixed ends) also has the distance, $d_0$ (as shown in **Figure 1** (**b**)). A voltage, $\Phi$, is applied across the compliant electrodes of the membrane and, a charge, $Q$, is built on the electrodes. The membrane is deformed from its passive equilibrium by $\Delta d$ (**Figure 1** (**c**)) and the total out-of-plane deformation of the membrane is $d = d_0 + \Delta d$.

The radial stretch of the membrane, $\lambda_1$, can be estimated based on the geometrical relationship,

$$\lambda_1 = \frac{\sqrt{d^2+(b-a)^2}}{(b-a)}\lambda_p \quad . \qquad \text{Eq. (1)}$$

Based on assumption (v), the circumferential stretch, $\lambda_2$, is simply $\lambda_2 = \lambda_p$.

The charge accumulated on the electrodes can be expressed as

$$Q = \pi(a+b)D\sqrt{d^2+(b-a)^2}, \qquad \text{Eq. (2)}$$

where $D$ is the electric displacement.

The DEO system is assumed to deform under an isothermal condition and the fixed temperature will not be considered explicitly. The DEO is a thermodynamic system with two independent variables: $d$ and $D$. Viscosity in the dielectric elastomer is considered in this system as the only dissipative factor. In this work, the Euler-Lagrange method is adopted to derive the governing equations of the DEO system (following [61] [62] [63] [64] [65]) and the Euler-Lagrange equations can be written as

$$\frac{\mathrm{d}}{\mathrm{d}t}\left(\frac{\partial L}{\partial \dot{q}_i}\right) - \frac{\partial L}{\partial q_i} = F_{NC\_i}, \qquad \text{Eq. (3)}$$

where $L = T - V$ is the Lagrangian, $T$ is the kinetic energy of the system and $V$ is the total potential energy of the system, $q_i = (d, D)$, $F_{NC\_i}$ are the nonconversative forces.

Assuming that the moving mass, $m$, is sufficiently larger than the mass of the springs and the DE

membrane, then the kinetic energy of the system, $T$, can be expressed as

$$T = \frac{1}{2} m \left(\frac{\mathrm{d}d}{\mathrm{d}t}\right)^2. \qquad \text{Eq. (4)}$$

The potential energy of this system, $V$, consists of the Helmholtz free energy of the dielectric elastomer membrane, the elastic potential energy of the springs and the potential energy of the external circuit, and is given as

$$V = \pi(b^2 - a^2)\frac{H_0}{\lambda_p^2} W + K(l - l_0)^2 - \Phi Q, \qquad \text{Eq. (5)}$$

where $W$ is the Helmholtz free energy density of the DE membrane, $K$ is the stiffness of the linear springs, $l_0$ is the initial length and $l = \sqrt{d^2 + h^2}$ is the current length of the springs under the deformation, $d$, and $h$ is the vertical distance from the fixed end of each spring to the axis of symmetry (as shown in **Figure 1** (**a**)).

By assuming an ideal elastomer, and that the polarization behaviour is liquid-like and independent of the state of deformation [66], the Helmholtz free energy density can be expressed as

$$W(\lambda, D) = W_{stretch}(\lambda) + \frac{D^2}{2\varepsilon}, \qquad \text{Eq. (6)}$$

where $\varepsilon$ is the permittivity, the first part on the right side is the free energy associated with the elastic energy of the membrane due to stretch and the second part is related to the electrostatic energy.

A Gent model [67] is adopted in this work to describe the hyper-elastic DE material and its Helmholtz free energy density is given as

$$W_{stretch}(\lambda) = -\frac{\mu J}{2} \log\left(1 - \frac{\lambda_1^2 + \lambda_2^2 + \lambda_1^{-2}\lambda_2^{-2} - 3}{J}\right), \qquad \text{Eq. (7)}$$

where $\mu$ is the shear modulus of the material and $J$ is the constant relating to the limiting stretch.

The generalized force in the Euler-Lagrange equation for variable $D$ equals zero as no electrical dissipation is considered in this work (e.g. leakage current). The generalized force for variable $d$ can be obtained by the virtual work principle. For a virtual displacement $\delta d$, the virtual work done by the viscosity of the DEO is (following [61] [68])

$$\delta W_{NC\_d} = -\frac{1}{2} c \lambda_p^2 \frac{d^2}{d^2 + r^2} \frac{\mathrm{d}d}{\mathrm{d}t} \delta d, \qquad \text{Eq. (8)}$$

where $c$ is the damping coefficient of the DE membrane and $r = b - a$.

Note that the viscoelastic behaviour of the DE membrane is simplified as a hyperelastic spring and a viscous damper in parallel, which is equivalent to the Kelvin-Voigt model. The Kelvin-Voigt model has been proven to be valid in characterizing the viscoelasticity of silicone elastomers (which is intended for this work) due to the significantly reduced stress relaxation and creep in comparison with the widely used VHB materials from 3M [31] [69] [70].

The virtual work can also be written as the product of the generalized force and the virtual displacement,

$$\delta W_{NC\_d} = F_{NC\_d} \delta d, \qquad \text{Eq. (9)}$$

where $F_{NC\_d}$ is the nonconservative generalized force for the variable $d$.

Substituting Eq. (9) into (8) yields

$$F_{NC\_d} = -\frac{1}{2}c\lambda_p^2 \frac{d^2}{d^2+r^2}\frac{\mathrm{d}d}{\mathrm{d}t}. \qquad \text{Eq. (10)}$$

The Euler-Lagrange equation for the variable $d$ can be written as

$$m\ddot{d} + \pi\mu(a+b)H_0\left(d/r\right)\frac{1-\frac{1}{\lambda_p^6\left(\left(d/r\right)^2+1\right)^2}}{1-\left(\lambda_p^2\left(\left(d/r\right)^2+1\right)+\lambda_p^2+\frac{1}{\lambda_p^4\left(\left(d/r\right)^2+1\right)}-3\right)/J} - \pi(a+b)\Phi D\frac{d}{\sqrt{d^2+r^2}} +$$

$$2Kd\left(1-\frac{l_0}{\sqrt{d^2+h^2}}\right) = -\frac{1}{2}c\lambda_p^2\frac{d^2}{d^2+r^2}\dot{d}. \qquad \text{Eq. (11)}$$

The Euler-Lagrange equation for the variable $D$ is

$$-\frac{H_0}{\lambda_p^2}\frac{D}{\varepsilon} + \Phi\frac{\sqrt{d^2+r^2}}{r} = 0. \qquad \text{Eq. (12)}$$

Substituting Eq. (12) to (11), and Eq. (11) can be nondimensionalized as

$$\frac{\mathrm{d}^2x}{\mathrm{d}\tau^2} + \frac{x\left(1-\frac{1}{\lambda_p^6(x^2+1)^2}\right)}{1-\left(\lambda_p^2(x^2+2)+\frac{1}{\lambda_p^4(x^2+1)}-3\right)/J} - x\tilde{\phi}^2 + \tilde{\kappa}x\left(1-\frac{l_0}{\sqrt{x^2r^2+h^2}}\right) + \tilde{c}\frac{x^2}{x^2+1}\frac{\mathrm{d}x}{\mathrm{d}\tau} = 0, \qquad \text{Eq. (13)}$$

where

$$\tau = t\sqrt{\frac{\pi\mu(a+b)H_0}{mr}},\ x = \frac{d}{r},\ \tilde{\phi} = \Phi\frac{\lambda_p}{H_0}\sqrt{\frac{\varepsilon}{\mu}},\ \tilde{k} = K\frac{2r}{\pi\mu(a+b)H_0},\ \tilde{c} = c\frac{\lambda_p^2}{2}\sqrt{\frac{r}{\pi\mu(a+b)H_0m}}\ .$$

Eq. (13) can be rewritten as

$$\frac{\mathrm{d}^2x}{\mathrm{d}\tau^2} + f\left(x,\lambda_p,\tilde{\phi},\tilde{k}\right) + \tilde{c}\frac{x^2}{x^2+1}\frac{\mathrm{d}x}{\mathrm{d}\tau} = 0, \qquad \text{Eq. (14)}$$

where

$$f\left(x,\lambda_p,\tilde{\phi},\tilde{k}\right) = \frac{x\left(1-\frac{1}{\lambda_p^6(x^2+1)^2}\right)}{1-\left(\lambda_p^2(x^2+2)+\frac{1}{\lambda_p^4(x^2+1)}-3\right)/J} - x\tilde{\phi}^2 + \tilde{\kappa}x\left(1-\frac{l_0}{\sqrt{x^2r^2+h^2}}\right)\ . \qquad \text{Eq. (15)}$$

In this work, the values of the Gent model parameters are determined based on the authors' previous ELASTOSIL silicone (Wacker Chemie AG) conical DEA studies [30] [31] [52]. The choice of using the material properties of silicone elastomers over common polyacrylate very-high-bond (VHB) tapes by 3M is due to the significantly lower viscosity of the silicone elastomers, which can generate much larger resonant stroke compared to VHB materials. For example, by using the same circular configuration, a silicone DEO [52] shows a nominal resonant stroke over five times higher than VHB counterparts [26]. The material parameters in this work are set as $\mu$ = 415.5 kPa and $J$ = 16, which are adopted from the authors' previous works [30] [31] [52]. The initial thickness of the elastomer, $H_0$, is 100 μm. The radius $a$ is set as 7.5 mm while $b$ is 15 mm. The permittivity, $\varepsilon$, is a product of the absolute permittivity of a vacuum and the relative permittivity of the dielectric

elastomer and is given as $\varepsilon = 2.48 \times 10^{-11}$ F/m. The mass is set as $m$ = 5 g, the initial length of the spring, $l_0$, is 10 mm and $h$ = 8 mm.

By solving the nondimensionalized equation-of-motion Eq. (14) numerically in MATLAB (MathWorks), the dynamic performance of the DEO system under small perturbation, high amplitude free oscillation and parametric mechanisms of excitation are investigated systemically in the following sections.

## 4. Stability of the static equilibrium states

This section focuses on the effects of pre-stretch ratios of the DE membranes, biasing DC voltages applied to the system and the stiffness of the biasing springs on the static equilibrium positions of the system and its natural frequency.

At the static equilibria, the static forces are balanced such that

$f(x_0, \lambda_p, \tilde{\phi}, \tilde{k}) = 0,$ Eq. (16)

where $x_0$ is the non-dimensional equilibrium position of the system.

By solving the Eq. (16) numerically, the non-dimensional equilibrium position, $x_0$, can be estimated with the known $\lambda_p$, $\tilde{\phi}$, $\tilde{k}$. The static stability of the equilibrium can be evaluated using the sign of the second derivative of Eq. (15) with respect to $x$, i.e. $\partial^2 f/\partial x^2|_{x_0}$. A positive sign indicates a stable equilibrium whereas a negative sign indicates an unstable one.

For low amplitude vibration around the equilibrium states, the time-dependent displacement can be written as

$x(\tau) = x_0 + \Delta(\tau),$ Eq. (17)

where $\Delta(\tau)$ is the amplitude of the small perturbation.

Substituting Eq. (17) into (14) (neglecting the damping term) and, expanding $f(x)$ as a power series in $\Delta$ around $x_0$ yields

$\frac{\mathrm{d}^2\Delta}{\mathrm{d}\tau^2} + \Delta \frac{\partial f(x,\lambda_p,\tilde{\phi},\tilde{k})}{\partial x} = 0.$ Eq. (18)

Note that the partial derivative in Eq. (18) is to be evaluated at the equilibrium $x_0$.

Hence the natural frequency of the DEA system is given as

$\tilde{\omega}_n^2 = \left.\frac{\partial f(x,\lambda_p,\tilde{\phi},\tilde{k})}{\partial x}\right|_{x=x_0},$ Eq. (19)

$\tilde{\omega}_n^2 = \frac{A_1A_2 - A_3A_4}{A_1^2} - \tilde{\phi}^2 + \tilde{k} - \frac{\tilde{k} l_0 h^2}{(x_0^2 r^2 + h^2)\sqrt{x_0^2 r^2 + h^2}},$ Eq. (20)

where $\tilde{\omega}_n = \omega_n \sqrt{\frac{mr}{\pi\mu(a+b)H_0}}$ is the non-dimensional natural angular frequency, and $A_{1\text{-}4}$ are written as

$A_1 = -\lambda_p^8 x_0^6 + (-4\lambda_p^8 + J\lambda_p^6 + 3\lambda_p^6)x_0^4 + (-5\lambda_p^8 + 2J\lambda_p^6 + 6\lambda_p^6 - 2\lambda_p^2)x_0^2 + (-2\lambda_p^8 + J\lambda_p^6 + 3J\lambda_p^6 - \lambda_p^2),$ Eq. (21 a)

$A_2 = 5J\lambda_p^6 x_0^4 + 6J\lambda_p^6 x_0^2 + J(\lambda_p^6 - 1),$ Eq. (21 b)

$$A_3 = J\lambda_p^6 x_0^5 + 2J\lambda_p^6 x_0^3 + J\left(\lambda_p^6 - 1\right)x_0, \qquad \text{Eq. (21 c)}$$
$$A_4 = -6\lambda_p^8 x_0^5 + 4\left(-4\lambda_p^8 + J\lambda_p^6 + 3\lambda_p^6\right)x_0^3 + 2\left(-5\lambda_p^8 + 2J\lambda_p^6 + 6\lambda_p^6 - 2\lambda_p^2\right)x_0. \qquad \text{Eq. (21 d)}$$

**Figure 2** (**a**) shows the stable equilibrium states of this system as a function of $\tilde{k}$ with the pre-stretch ratios $\lambda_p$ = 1.0, 1.2 and 1.4. The biasing DC voltage is set as zero in this study. A clear supercritical pitchfork bifurcation with respect to $\tilde{k}$ can be observed in **Figure 2** (**a**). For $\lambda_p$ = 1.0, regardless of the value of $\tilde{k}$, two stable equilibria exist whereas, for the pre-stretch ratios of 1.2 and 1.4, only a single equilibrium point on the origin exists for small $\tilde{k}$ values. As the $\tilde{k}$ value increases, this stable equilibrium curve bifurcates with two symmetrical stable equilibria emerging, whilst the origin becomes an unstable equilibrium (dashed line in **Figure 2** (**a**)). As the pre-stretch ratio increases, the bifurcation also occurs at a higher $\tilde{k}$ value. **Figure 2** (**b**) shows the relationship between the natural frequency of the DEO and the non-dimensional stiffness $\tilde{k}$ for different pre-stretch ratios. For $\lambda_p$ = 1.0, the natural frequency increases continuously with the increasing $\tilde{k}$ while, for $\lambda_p$ = 1.2 and 1.4, the natural frequency decreases to zero as the $\tilde{k}$ value approaches the corresponding bifurcation point, and then increases gradually.

The effect of the biasing DC voltage on the static equilibrium positions and natural frequencies was also investigated, with $\tilde{k}$ set as 2.5. **Figure 2** (**c**) and (**d**) shows the stable equilibria and natural frequencies of the DEO system respectively with $\lambda_p$ = 1.0, 1.2 and 1.4. It can be noted that, for $\lambda_p$ = 1.0 which has a bistability, as the biasing voltage increases, the absolute values of the two symmetrical stable equilibria, and the corresponding natural frequencies, increase. Both the $\lambda_p$ = 1.2 and 1.4 cases exhibit a monostability at low $\tilde{\phi}$ values; however, a supercritical pitchfork bifurcation occurs in the $\lambda_p$ = 1.2 case as $\tilde{\phi}$ increases beyond 0.235 while $\lambda_p$ = 1.4 remains monostable even when $\tilde{\phi}$ approaches its maximum. The natural frequency of the system in the $\lambda_p$ = 1.2 case drops to its minimum at the bifurcation point before rising. As the system remains monostable, the natural frequency for the $\lambda_p$ = 1.4 case decreases gradually with the increasing biasing voltage.

The studies in this section illustrate a transition between a monostability and a bistability in the system by a biasing voltage control and tuning the design parameters ($\tilde{k}$, $\lambda_p$). They demonstrate that, with the correct choice of parameters values (e.g. $\lambda_p$ = 1.2, $\tilde{k} = 2.5$), the system can exhibit a planar configuration ($x$ = 0) in passive (no voltage) and a conical geometry when a biasing voltage is applied. In quasi-static applications, this novel DEO system can have potential advantages in changing active morphology and in compliant linear actuators with programmable stroke ranges.

## 5. Free oscillation of the DEO

In the previous section, the static equilibrium states and the natural frequencies for low amplitude oscillations, due to small perturbations around the static equilibria, were analysed. In this section, the dynamics of the DEO system under a high amplitude free oscillation is investigated. The conservative case, i.e. no forcing or viscous damping, is considered first, then the nonconservative effects of damping on the dynamics are analysed.

### 5.1 Conservative case

In the first study, a conservative system is considered by neglecting the damping term in Eq. (14) and applying only a constant DC biasing voltage to the DEO (no periodic forcing). This system becomes *autonomous*, i.e. time-independent. In the last section, the case $\lambda_p$ = 1.2, $\tilde{k}$ = 2.5 showed that a supercritical pitchfork bifurcation in the static equilibria can be controlled by the DC voltage. By adopting the parameters from that study, free oscillations of the DEO under different amplitudes of biasing voltages are analysed.

**Figure 3** (**a-c**) plots the potential energy of this system and the phase portraits with $\tilde{\phi}$ = 0, 0.25 and 0.5 respectively. It can be seen that, when $\tilde{\phi}$ = 0, only one minimum exists in the potential energy function, and $x$ = 0 represents the only *centre* of the system. For this conservative system, depending on the level of the total mechanical energy, $\tilde{E}_m = \tilde{V} + \tilde{T}$, oscillations occur on different orbits around the single *fixed point* (0, 0), as demonstrated in **Figure 3** (**a**). As $\tilde{\phi}$ is increased to 0.25, which is slightly above the bifurcation point of $\tilde{\phi} = 0.235$, the potential energy function forms a symmetrical twin-well curve. It can be noted that two symmetrical minima of the potential energy function occur near the origin (green dots in **Figure 3** (**b**)), and the origin becomes a local maximum (red dot in **Figure 3** (**b**)). The two minima represent the stable equilibrium points (centres) and the local maximum indicates an unstable equilibrium (*saddle*). Two symmetric homoclinic orbits can be observed in the phase portraits in **Figure 3** (**b**), which separate the low amplitude intra-well orbits around each of the stable equilibrium points from the high amplitude inter-well orbits that enclose both. As the non-dimensional voltage value increases, the two stable equilibrium points separate further, the homoclinic orbits grow and a higher energy is required to escape from one potential well to the other, as is shown in **Figure 3** (**c**).

The time series of the DEO system with different total mechanical energy levels for $\tilde{\phi} = 0.5$ are plotted in **Figure 4** (**a-c**), where the blue dotted lines represent the two stable equilibria (centres, $x_{c+}$ and $x_{c-}$) and the red dotted line illustrates the unstable solution (saddle, $x_s$). As the total energy is below zero (initial condition: $x = 0.2$, $\dot{x} = 0$), the system demonstrates a low amplitude intra-well oscillation around the corresponding equilibrium (depending on the initial position). When the total energy is close to zero, the system transits from an intra-well oscillation ($\tilde{E}_m < 0$, solid curve in **Figure 4** (**b**)) to an inter-well oscillation ($\tilde{E}_m > 0$, dashed curve in **Figure 4** (**b**)). As the total mechanical energy increases further, the response of the system shows a high amplitude inter-well oscillation, as illustrated in **Figure 4** (**c**).

### 5.2 Nonconservative case

When the damping term in Eq. (14) is considered, this system is no longer conservative, i.e. as the system oscillates, the total mechanical energy dissipates and the system eventually settles on the positions with the minimum potential energy. This can be seen from the phase portraits in **Figure 5** where, with the presence of damping, the system response in a free oscillation no longer has a closed orbit around the centres, but rather is attracted to the stable equilibria, which are also called *attractors*. Also note from **Figure 5** (**a**) that, in the case of $\tilde{\phi} = 0$, where the system is monostable, only a single attractor exists and different initial conditions are drawn to the same equilibrium point (marked as black dot in **Figure 5** (**a**)). However, in the $\tilde{\phi} = 0.5$ case, where the system is bistable,

a small variation in the initial condition can lead to a different equilibrium point (marked as black dots in **Figure 5** (**b**)).

To map the initial conditions that are attracted to the two equilibrium points in the $\tilde{\phi} = 0.5$ case, a *cell-to-cell mapping* technique [71] is adopted by dividing the initial condition region of interest into grids and numerically computing the final equilibrium point that each initial condition lands on. *Basins of attraction*, that characterize the eventual, steady state behaviour of this oscillator, can be obtained using this technique. In this study, the initial displacement and velocity are varied from -1 to 1 over 200 points with a fixed step, which lead to a total of $200 \times 200$ cells. The effects of damping on the basins of attraction are also investigated in this study. The basins of attraction for the two attractors in the cases of $\tilde{c}$ = 0.1, 0.5 and 1.0 are shown in **Figure 6** (**a-c**) respectively. The black and white regions indicate the initial conditions that asymptotically tend to the equilibrium point on the left side ($x$ = -0.31) and right side ($x$ = 0.31) respectively. It can be noted that the basins of attraction plotted in **Figure 6** follow a spiral pattern and, as the damping in the system increases, the basins of attraction concentrate more and become wider, indicating that broader neighbouring initial conditions can settle on the same equilibrium point.

## 6. Effects of parametric excitation

In the previous sections, the voltage excitation term in Eq. (14) contained only a fixed biasing DC voltage. In this section, we focus on the nonlinear dynamics of the DEO system when subjected to a time varying voltage signal. Note that the forcing term of this system is a function of the displacement (Eq. (14)), hence this system is excited parametrically [18] [19]. It is noteworthy that the forcing term is also a function of the square of the voltage input (Eq. (14)). Therefore, for a voltage signal given as $\tilde{\phi} = \tilde{\phi}_{DC} + \tilde{\phi}_{AC}\cos(\widetilde{\Omega}\tau)$, where $\tilde{\phi}_{DC}$ and $\tilde{\phi}_{AC}$ are the DC and AC voltage amplitudes respectively, and $\widetilde{\Omega} = \Omega\sqrt{\frac{mr}{\pi\mu(a+b)H_0}}$ is the non-dimensional angular excitation frequency, the force experienced by the moving mass is proportional to

$$\tilde{\phi}^2 = E_a + E_b\cos(\widetilde{\Omega}\tau) + E_c\cos(2\widetilde{\Omega}\tau) \ , \qquad \text{Eq. (22)}$$

where

$E_a = \tilde{\phi}_{DC}^2 + \frac{\tilde{\Phi}_{AC}^2}{2}$ ,

$E_b = 2\tilde{\phi}_{DC}\tilde{\phi}_{AC}$ ,

$E_c = \frac{\tilde{\phi}_{AC}^2}{2}$ .

From Eq. (22) it can be noted that the forcing term contains one constant biasing component and two time-varying components: one at the input excitation frequency and the second is at twice of the input frequency. However, it should be noted that, for low AC-to-DC ratio, i.e. $ADR = \tilde{\phi}_{AC}/\tilde{\phi}_{DC}$ values (e.g. < 0.25), the amplitude of the frequency-doubled forcing component, $E_c$, is over one order of magnitude smaller than the primary forcing component, $E_b$, hence can be neglected. It is worth noting that both the DC and AC voltage amplitudes contribute to the biasing forcing component, $E_a$. In previous DEA dynamic studies, the effects of *ADR* in the voltage signal on the dynamic responses was investigated via varying $\tilde{\phi}_{AC}$ while fixing the biasing voltage $\tilde{\phi}_{DC}$ [23] [52] [62] [72]. However, as shown in Eq. (22), despite the control in the biasing voltage, such a

method can still cause a change in the biasing excitation component, which leads to a shift in the equilibrium point, and hence the resonant behaviour. To overcome this drawback, in this work, the effects of *ADR* are investigated by fixing the biasing excitation term (i.e. $E_a = const$) while tuning the *ADR* value.

### 6.1 Small *ADR* values

In the last section, the transition from monostability to bistability in the DEO system via a biasing voltage control was demonstrated. The same design parameters are adopted here ($\lambda_p = 1.2$, $\tilde{k} = 2.5$) and the damping coefficient $\tilde{c}$ is set as 0.25. As shown in **Figure 3**, the transition in stability occurs at a biasing voltage $\tilde{\phi}_{DC} = 0.235$, which corresponds to a biasing forcing component $E_a = \tilde{\phi}_{DC}^2 = 0.235^2$ (note that in Section 5 the biasing forcing component is only a function of $\tilde{\phi}_{DC}$ as $\tilde{\phi}_{AC} = 0$). In the first study, we investigate the response of the DEO with different *ADR* values in two cases. In the case **i**, the biasing forcing component $E_a = \tilde{\phi}_{DC}^2 + \tilde{\phi}_{AC}^2/2 = 0.2^2$ (where the system has a single stable equilibrium point) and in case **ii**, $E_a = 0.5^2$ (where the system has two stable symmetrical equilibrium points). The *ADR* value in this study is restricted to a very small value ($ADR < 0.04$), which ensures an intra-well oscillation for case **ii**, while the high amplitude inter-well oscillation is analysed in the next subsection.

The frequency response of the DEO system is shown in **Figure 7** (**a**) and (**b**) for the $E_a = 0.2^2$ and $E_a = 0.5^2$ cases respectively. The amplitude, $|X_r|$, is defined as $|X_r| = |X_{max} - X_{min}|/2$, where $X_{max}$ and $X_{min}$ are the maximum and minimum displacement in one complete cycle respectively. Note that the frequency response curves are obtained using the MATLAB-based continuation package Computational Continuation Core (COCO) (a more detailed introduction to this software package can be found in [73]). A clear resonant peak can be observed for both cases, where the response curve for case **i** is shifted to the right, representing a hardening system (the stiffness of the system increases with the increasing displacement). On the contrary, the response curve for case **ii** exhibits a leftwards shift, suggesting a softening system.

It is worth noting that, in case **i**, the system exhibits a zero-amplitude response away from resonance. As the excitation frequency approaches the resonant frequency, a *Hopf* bifurcation occurs (as indicated by the stars in **Figure 7** (**a**)) and the response transitions from no motion to large-amplitude periodic oscillation. At this *Hopf* bifurcation, the zero-amplitude solution loses stability, hence the only stable solutions between the two *Hopf* bifurcations are periodic oscillations. If the excitation frequency is increased gradually from below resonance (e.g. $\tilde{\Omega} < 0.2$), the response will follow the solid upper branch and, as it reaches the *fold point* (circles in **Figure 7** (**a**)), the response loses its stability and *drops down* to zero. Multiple solutions can exist across a wide range of the frequency response in **Figure 7** (**a**), where the solid upper branch represents a stable solution while the dashed curve indicates an unstable one. As the *ADR* value increases, the peak amplitude and the peak frequency (corresponding frequency of the circle in **Figure 7** (**a**)) also increase.

The frequency response for case **ii** ($E_a = 0.5^2$) shows a completely different behaviour to case **I** ($E_a = 0.2^2$). In case **ii**, the system demonstrates non-zero-amplitude periodic responses away from resonance. By increasing the excitation frequency in a quasi-static manner from below resonance (e.g. $\tilde{\Omega} < 0.2$), the response will follow the solid lower branch and, as it reaches the first fold point

(circles in **Figure 7** (**b**)), the response will *jump up* to the upper branch. Decreasing the excitation frequency from above the resonance will cause the system response to follow the upper solid branch with higher amplitudes and then drop down at the fold point. Note from **Figure 7** (**b**) that an increase in the *ADR* value causes the peak amplitude to increase, but decreases the peak frequency. It is noteworthy that period-doubling, which potentially leads to chaos, was predicted for *ADR* = 0.02 and 0.03 cases. However, due to the complex nature of these behaviours, detailed study of the period-doubling bifurcations and the roots to chaos are beyond the scope of this paper. Additionally, as demonstrated later in **Figure 9**, the chaotic region is relatively small and the system may be operated on either side of this region without needing to take it into account.

The time histories of the voltage input and displacement output for both cases at $\widetilde{\Omega} = 0.45$ and *ADR* = 0.02 are illustrated in **Figure 8** (**a**) and (**c**) respectively. In both cases, the system experiences resonances at $\widetilde{\Omega} = 0.45$ with a comparable amplitude. However, the two cases demonstrate different forcing-to-response period ratios. For case **i**, the response period is twice that of the forcing period (**Figure 8** (**a**)) while case **ii** shows a 1:1 relationship between the periods (**Figure 8** (**c**)). The phase portraits and Poincaré maps for case **i** are shown in **Figure 8** (**b**) and are plotted based on the state space data in 100 forcing cycles. Note that the phase paths and Poincaré maps overlap with each other, showing a periodic response. The two Poincaré sections also suggest that the response repeats itself every two forcing periods. The overlap in the phase path and Poincaré section for case **ii** in **Figure 8** (**d**) also indicates that this system undergoes a periodic response.

### 6.2 Large *ADR* values

In the previous study, the frequency response of the DEO system under a parametric excitation with low *ADR* value was investigated. By increasing the *ADR* value, the monostable system is expected to exhibit a continuously increasing resonant amplitude, as has been demonstrated in previous work [52]. However, for a bistable system with twin potential wells, the increase in *ADR* value results in a higher periodic forcing amplitude which means a higher energy input to the system. The higher energy input could then lead to an increase in the total mechanical energy of the DEO, especially near resonance. Once the total mechanical energy is greater than the depth of the potential wells, the intra-well response can transit to a high amplitude inter-well oscillation. Hence, in this study, we focus on the bistable case ($E_a = 0.5^2$).

A frequency sweep from $\widetilde{\Omega} = 0$ to $\widetilde{\Omega} = 1.6$ with an *ADR* = 0.2 was conducted and the time histories are shown in **Figure 9**. It can be noted that, at low frequencies, the DEO system experiences intra-well oscillations with a small peak at point **a**. As the frequency increases, the oscillation amplitude also increases, as the amplitude passes the threshold of the depth of the well (red dash line in **Figure 9**), the system transitions to inter-well oscillation, but first in a chaotic manner (point **b**) then settles to steady periodic oscillations (point **c**). The time series, phase portraits and Poincaré maps for each point are also included in **Figure 9**. It is noteworthy that the Poincaré maps for point **b** are disordered, indicating an aperiodic response, while the Poincaré maps for the other two points are overlapped, which shows a periodic behaviour. Also note that the response period for point **c** is twice of the forcing period, demonstrating a period-doubling response.

## 7. Oscillation control of the DEO system

In the previous section, both intra- and inter-well oscillations of the DEO system in a bistable mode have been demonstrated when it is subjected to different excitation signals. In practical applications, it is desirable to have the oscillation controllable - in particular, to be capable of switching between oscillations around different equilibria via a simple voltage control. Such active control could lead to more advanced vibrational control and dynamic shape morphing. In this section, a simple active control strategy for this DEO system based on the basins of attraction is proposed and an example demonstrating the effectiveness of this control strategy is presented.

The same design parameters are adopted from the previous section ($\lambda_p = 1.2$, $\tilde{k} = 2.5$, $\tilde{c} = 0.25$). A biasing forcing component of $E_a = 0.5^2$ is kept which ensures the system stays in a bistable mode. One of the control difficulties for this DEO system lies in the transition from inter-well to intra-well oscillation as there is an equal possibility for the system to be attracted to the two symmetrical equilibria. In this work, the voltage is controlled to ensure that the response reliably reaches a target equilibrium point. This uses the concept of basins of attraction, illustrated in **Figure 6** - i.e. that particular initial conditions cause the system to settle on particular equilibrium points. If the excitation is "switched off" mid-way through an orbit, the states at that point will then represent the initial conditions for the decay. This allows specific initial conditions to be reached, and thus allows the individual equilibrium points to be targeted.

If a periodic inter-well orbit (avoiding the chaotic region) is used as the initial response, only the states in one response cycle are required to reach either of the equilibria (rather than computing the entire map, as in **Figure 6**). Such a map, for the DEO at $ADR = 0.25$ and $\tilde{\Omega} = 0.9$ is shown in **Figure 10** (**a**) where the orbit formed by alternating red and blue dots represents the periodic inter-well response of the system and blue and red sections correspond to a final steady state response on attractor (equilibrium point) $x_{A+}$ and $x_{A-}$ respectively. Examples of the phase portraits and time histories of the DEO exhibiting a controlled behaviour, settling on each of the attractors, are plotted in **Figure 10** (**a-b**) and (**c-d**) respectively. The large black arrows in the phase portraits in **Figure 10** (**a** & **c**) depict the start point of the oscillation control. The white regions in **Figure 10** (**b** & **d**) represent the parametrically excited periodic oscillations of the DEO while the shaded regions indicate the voltage regulation (setting $ADR$ to 0 while keeping $E_a = 0.5^2$) to allow the responses to reach the targeted equilibrium. It can be noted from **Figure 10** (**a** & **c**) that the system which has its states in the blue (red) section on the orbit is successfully attracted to the equilibrium in blue (red) by using this control strategy. Once the system has settled on the desired equilibrium, an AC voltage with a lower $ADR$ (to ensure an intra-well oscillation) can be applied to the DEO to perform intra-well oscillations. It is worth noting that, in practical applications, this control strategy may require a set of high sampling rate devices to track its states (displacement and velocity) and to perform voltage regulation. For the case with $\tilde{\Omega} = 0.9$, the dimensional excitation frequency is 45 Hz, which may require a sampling rate in the order of $10^4$ Hz, which is believed to be realistic for practical applications.

To demonstrate the use of this strategy for DEO oscillation control, an example is developed where the system has the following desired oscillation sequences: **i**. intra-well oscillation around $x_{A+}$; **ii**. high amplitude inter-well oscillation; **iii**. intra-well oscillation around $x_{A-}$; **iv**. inter-well oscillation

and, finally, **v**. land on $x_{A+}$. In this example, the *ADR* ratio of 0.02 and $\widetilde{\Omega} = 0.5$ are used for intra-well oscillation and *ADR* ratio of 0.25 and $\widetilde{\Omega} = 0.9$ are adopted for inter-well oscillation. The time histories of the actuation voltage parameters and the corresponding DEO responses are plotted in **Figure 11**. The dark shaded areas represent the triggering of the position control strategy developed in this section. It can be noted that the system response follows the desired oscillation sequence successfully with a short transient period after the change of actuation voltage parameters each time. Note that, in this example, all parameters are demonstrated in their non-dimensional form. To give a direct overview of such system, these parameters are now converted to the ones with dimensions, as listed below. For the DEO with $H_0$ = 100 μm, $a$ = 7.5 mm, $b$ = 15 mm, $\lambda_p$ = 1.2. The excitation frequency for intra-well oscillations is $f$ = 25 Hz, and is $f$ = 45 Hz for inter-well oscillations. The excitation frequencies are well within the output range of the state-of-the-art high voltage power electronics, which demonstrates the feasibility of using this DEO design in practical applications such as vibrational robot locomotion.

## 8. Conclusion

In this work, a novel conical dielectric elastomer oscillator with a bistable biasing mechanism was developed. This DEO configuration breaks the restriction of fixed stability of previous DEO designs, as this system can switch from a monostability to a bistability via a simple voltage control. A theoretical model was derived using the Euler-Lagrange method to characterize the responses of this DEO system. Using this model the static equilibrium states, and their stability, were investigated. Additionally, the free oscillation responses, the effects of damping and parametric excitation were explored. A simple control strategy was proposed to allow an accurate transitions between oscillations about different equilibria. The key findings of this work are summarized as follows:

i. This DEO system can exhibit either a monostability or a bistability, which can be controlled by a biasing voltage and tuning of the design parameters.
ii. In monostable mode, the DEO system exhibits zero displacement for excitation away from resonant frequencies but high amplitude oscillations near resonance with a double-period response.
iii. In bistable mode, two symmetrical stable equilibrium points are observed in the DEO system. Low amplitude intra-well orbits, around each of the equilibrium points, and high amplitude inter-well orbits that enclose both, are observed in undamped free oscillations.
iv. The basins of attraction of the bistable DEO system demonstrate that different initial conditions cause the system to settle on different equilibrium points.
v. When the bistable DEO system is excited, it exhibits only intra-well oscillations at low *ADR* with a 1:1 period response. Chaotic and period-doubling inter-well responses are observed as the *ADR* increases.
vi. The transition from periodic inter-well to intra-well oscillations around the target equilibrium in the bistable DEO system can be achieved with the use of the attractor map and a voltage control.

In quasi-static cases, this DEO design can morph from a planar configuration to a three-dimensional conical geometrical profile using a simple static voltage control. This morphing behaviour can have applications such as active morphing wings on aircraft or working as a compliant linear actuator

with a programmable working range. In dynamic applications, the controllability of this DEO design allows a programmable oscillation around the targeted equilibrium, which could lead to more advanced and versatile DEO applications such as active vibrational control, smart energy harvesting and highly programmable robotic locomotion. The transition from one equilibrium to the other, as demonstrated in Section 7, also offers a new solution for bridging the energy gap to transition between two equilibria in a bistable system by using vibration, rather than the requirement for a large force.

## Acknowledgement

C.C., B.L., and X.G. appreciates support from The National Key Research and Development Program of China (2019YFB1311600). B.L. acknowledges the National Natural Science Foundation of China for support (Grant No. 91748124). L.W. appreciates support from the National Natural Science Foundation of China (Grant No. U1713219). X.G. thanks the Shenzhen Engineering Laboratory for Key Technologies on Intervention Diagnosis and Treatment Integration.

## References

[1] R. Pelrine, R. Kornbluh, Q. Pei, and J. Joseph, "High-speed electrically actuated elastomers with strain greater than 100%," *Science (80-. ).*, vol. 287, no. 5454, pp. 836–839, 2000.

[2] G. Kovacs, L. Düring, S. Michel, and G. Terrasi, "Stacked dielectric elastomer actuator for tensile force transmission," *Sensors Actuators, A Phys.*, vol. 155, no. 2, pp. 299–307, 2009.

[3] C. T. Nguyen *et al.*, "A small biomimetic quadruped robot driven by multistacked dielectric elastomer actuators," *Smart Mater. Struct.*, vol. 23, no. 6, 2014.

[4] H. S. Jung, K. H. Cho, J. H. Park, and S. Y. Yang, "Musclelike joint mechanism driven by dielectric elastomer actuator for robotic applications," *Smart Mater. Struct.*, vol. 27, no. 7, p. 075011, 2018.

[5] M. Hodgins, G. Rizzello, D. Naso, A. York, and S. Seelecke, "An electro-mechanically coupled model for the dynamic behavior of a dielectric electro-active polymer actuator," *Smart Mater. Struct.*, vol. 23, no. 10, p. 104006, 2014.

[6] X. Li, W. Li, W. Zhang, H. Zou, Z. Peng, and G. Meng, "Magnetic force induced tristability for dielectric elastomer actuators," *Smart Mater. Struct.*, vol. 26, no. 10, p. 105007, 2017.

[7] A. T. Conn and J. Rossiter, "Towards holonomic electro-elastomer actuators with six degrees of freedom," *Smart Mater. Struct.*, vol. 21, no. 3, p. 035012, 2012.

[8] Q. Pei, M. Rosenthal, S. Stanford, H. Prahlad, and R. Pelrine, "Multiple-degrees-of-freedom electroelastomer roll actuators," *Smart Mater. Struct.*, vol. 13, no. 5, pp. N86–N92, 2004.

[9] G. K. Lau, H. T. Lim, J. Y. Teo, and Y. W. Chin, "Lightweight mechanical amplifiers for rolled dielectric elastomer actuators and their integration with bio-inspired wing flappers," *Smart Mater. Struct.*, vol. 23, no. 2, p. 025021, 2014.

[10] H. Zhao, A. M. Hussain, M. Duduta, D. M. Vogt, R. J. Wood, and D. R. Clarke, "Compact Dielectric Elastomer Linear Actuators," *Adv. Funct. Mater.*, vol. 28, no. 42, p. 1804328, 2018.

[11] G. Kofod, W. Wirges, M. Paajanen, and S. Bauer, "Energy minimization for self-organized structure formation and actuation," *Appl. Phys. Lett.*, vol. 90, no. 8, pp. 1–4, 2007.

[12] S. Shian, K. Bertoldi, and D. R. Clarke, "Dielectric Elastomer Based 'grippers' for Soft

Robotics," *Adv. Mater.*, vol. 27, no. 43, pp. 6814–6819, 2015.

[13] O. A. Araromi *et al.*, "Rollable multisegment dielectric elastomer minimum energy structures for a deployable microsatellite gripper," *IEEE/ASME Trans. Mechatronics*, vol. 20, no. 1, pp. 438–446, 2015.

[14] G. K. Lau, K. R. Heng, A. S. Ahmed, and M. Shrestha, "Dielectric elastomer fingers for versatile grasping and nimble pinching," *Appl. Phys. Lett.*, vol. 110, no. 18, 2017.

[15] D. Rus and M. T. Tolley, "Design, fabrication and control of soft robots," *Nature*, vol. 521, no. 7553, pp. 467–475, 2015.

[16] J. W. Fox and N. C. Goulbourne, "On the dynamic electromechanical loading of dielectric elastomer membranes," *J. Mech. Phys. Solids*, vol. 56, no. 8, pp. 2669–2686, 2008.

[17] J. W. Fox and N. C. Goulbourne, "Electric field-induced surface transformations and experimental dynamic characteristics of dielectric elastomer membranes," *J. Mech. Phys. Solids*, vol. 57, no. 8, pp. 1417–1435, 2009.

[18] J. Zhu, S. Cai, and Z. Suo, "Resonant behavior of a membrane of a dielectric elastomer," *Int. J. Solids Struct.*, vol. 47, no. 24, pp. 3254–3262, 2010.

[19] J. Zhu, S. Cai, and Z. Suo, "Nonlinear oscillation of a dielectric elastomer balloon," *Polym. Int.*, vol. 59, no. 3, pp. 378–383, 2010.

[20] J. Zhang, H. Chen, B. Li, D. McCoul, and Q. Pei, "Coupled nonlinear oscillation and stability evolution of viscoelastic dielectric elastomers," *Soft Matter*, vol. 11, no. 38, pp. 7483–7493, 2015.

[21] J. Zhang, H. Chen, and D. Li, "Nonlinear Dynamical Model of a Soft Viscoelastic Dielectric Elastomer," *Phys. Rev. Appl.*, vol. 8, no. 6, p. 064016, 2017.

[22] T. Li, S. Qu, and W. Yang, "Electromechanical and dynamic analyses of tunable dielectric elastomer resonator," *Int. J. Solids Struct.*, vol. 49, no. 26, pp. 3754–3761, 2012.

[23] B. Li, J. Zhang, L. Liu, H. Chen, S. Jia, and D. Li, "Modeling of dielectric elastomer as electromechanical resonator," *J. Appl. Phys.*, vol. 116, no. 12, p. 124509, 2014.

[24] B. Li, J. Zhang, H. Chen, and D. Li, "Voltage-induced pinnacle response in the dynamics of dielectric elastomers," *Phys. Rev. E*, vol. 93, no. 5, p. 052506, 2016.

[25] L. Liu, B. Li, W. Sun, H. Chen, and D. Li, "Viscoelastic effect and creep elimination of dielectric elastomers in adversarial resonance," *J. Appl. Phys.*, vol. 120, no. 16, p. 164502, 2016.

[26] C. Tang, B. Li, W. Sun, Z. Li, and H. Chen, "Identification and characterization of the out-of-plane resonance in a dielectric elastomer to drive an agile robotic cube," *J. Appl. Phys.*, vol. 122, no. 16, p. 165104, 2017.

[27] C. Tang, B. Li, H. Fang, Z. Li, and H. Chen, "A speedy, amphibian, robotic cube: Resonance actuation by a dielectric elastomer," *Sensors Actuators, A Phys.*, vol. 270, pp. 1–7, 2018.

[28] G. Gu, U. Gupta, J. Zhu, L. Zhu, and X. Zhu, "Feedforward deformation control of a dielectric elastomer actuator based on a nonlinear dynamic model," *Appl. Phys. Lett.*, vol. 107, no. 4, p. 042907, 2015.

[29] G. Gu, U. Gupta, J. Zhu, L. Zhu, and X. Zhu, "Modeling of Viscoelastic Electromechanical Behavior in a Soft Dielectric Elastomer Actuator," *IEEE Trans. Robot.*, vol. 33, no. 5, pp. 1263–1271, 2017.

[30] C. Cao, X. Gao, and A. T. Conn, "A compliantly coupled dielectric elastomer actuator using magnetic repulsion," *Appl. Phys. Lett.*, vol. 114, no. 1, p. 011904, 2019.

[31] C. Cao, T. L. Hill, A. T. Conn, B. Li, and X. Gao, “Nonlinear Dynamics of a Magnetically Coupled Dielectric Elastomer Actuator,” *Phys. Rev. Appl.*, vol. 12, no. 4, p. 044033, 2019.

[32] J. Zhao *et al.*, “Bistable dielectric elastomer minimum energy structures,” *Smart Mater. Struct.*, vol. 25, no. 7, p. 075016, 2016.

[33] Y. Wang, U. Gupta, N. Parulekar, and J. Zhu, “A soft gripper of fast speed and low energy consumption,” *Sci. China Technol. Sci.*, vol. 62, no. 1, pp. 31–38, 2019.

[34] W. Li, W. Zhang, H. Zou, Z. Peng, and G. Meng, “A Fast Rolling Soft Robot Driven by Dielectric Elastomer,” *IEEE Trans. Mechatronics*, vol. 23, no. 4, pp. 1630–1640, 2018.

[35] M. Duduta, D. R. Clarke, and R. J. Wood, “A high speed soft robot based on dielectric elastomer actuators,” *2017 IEEE Int. Conf. Robot. Autom.*, pp. 4346–4351, 2017.

[36] T. Li *et al.*, “Agile and Resilient Insect-Scale Robot,” *Soft Robot.*, vol. 6, no. 1, pp. 133–141, 2018.

[37] J. Zhao, J. Niu, D. McCoul, Z. Ren, and Q. Pei, “Phenomena of nonlinear oscillation and special resonance of a dielectric elastomer minimum energy structure rotary joint,” *Appl. Phys. Lett.*, vol. 106, no. 13, p. 133504, 2015.

[38] C. Cao, R. S. Diteesawat, J. Rossiter, and A. T. Conn, “A Reconfigurable Crawling Robot Driven by Electroactive Artificial Muscle,” in *2019 2nd IEEE International Conference on Soft Robotics (RoboSoft)*, 2019, pp. 840–845.

[39] Y. Chen *et al.*, “Controlled flight of a microrobot powered by soft artificial muscles,” *Nature*, vol. 575, 2019.

[40] C. Cao, X. Gao, and A. T. Conn, “A Magnetically Coupled Dielectric Elastomer Pump for Soft Robotics,” *Adv. Mater. Technol.*, vol. 4, no. 8, p. 1900128, 2019.

[41] X. Gao, C. Cao, J. Guo, and A. T. Conn, “Elastic Electroadhesion with Rapid Release by Integrated Resonant Vibration,” *Adv. Mater. Technol.*, vol. 4, no. 1, p. 1800378, 2019.

[42] C. Keplinger, J.-Y. Sun, C. C. Foo, P. Rothemund, G. M. Whitesides, and Z. Suo, “Stretchable, Transparent, Ionic Conductors,” *Science (80-. ).*, vol. 341, no. 6149, pp. 984–987, 2013.

[43] Z. Lu, H. Godaba, Y. Cui, C. C. Foo, M. Debiasi, and J. Zhu, “An electronically tunable duct silencer using dielectric elastomer actuators,” *J. Acoust. Soc. Am.*, vol. 138, no. 3, pp. EL236–EL241, 2015.

[44] P. Rothemund, X. P. Morelle, K. Jia, G. M. Whitesides, and Z. Suo, “A Transparent Membrane for Active Noise Cancelation,” *Adv. Funct. Mater.*, vol. 28, no. 29, pp. 1–8, 2018.

[45] R. SARBAN, R. W. JONES, E. RUSTIGHI, and B. R. MACE, “Active Vibration Isolation Using a Dielectric Electro-Active Polymer Actuator,” *J. Syst. Des. Dyn.*, vol. 5, no. 5, pp. 643–652, 2011.

[46] Y. Zhao, Q. Guo, S. Wu, G. Meng, and W. Zhang, “Design and experimental validation of an annular dielectric elastomer actuator for active vibration isolation,” *Mech. Syst. Signal Process.*, vol. 134, p. 106367, 2019.

[47] T. Li, C. Keplinger, R. Baumgartner, S. Bauer, W. Yang, and Z. Suo, “Giant voltage-induced deformation in dielectric elastomers near the verge of snap-through instability,” *J. Mech. Phys. Solids*, vol. 61, no. 2, pp. 611–628, 2013.

[48] F. Chen and M. Y. Wang, “Dynamic performance of a dielectric elastomer balloon actuator,” *Meccanica*, vol. 50, no. 11, pp. 2731–2739, 2015.

[49] G. Rizzello, M. Hodgins, D. Naso, A. York, and S. Seelecke, “Dynamic Modeling and Experimental Validation of an Annular Dielectric Elastomer Actuator With a Biasing Mass,” *J.*

*Vib. Acoust.*, vol. 137, no. 1, p. 011005, 2015.

[50] J. Zou, G. Y. Gu, and L. M. Zhu, "Open-loop control of creep and vibration in dielectric elastomer actuators with phenomenological models," *IEEE/ASME Trans. Mechatronics*, vol. 22, no. 1, pp. 51–58, 2017.

[51] J. Zou and G. Gu, "High-precision tracking control of a soft dielectric elastomer actuator with inverse viscoelastic hysteresis compensation," *IEEE/ASME Trans. Mechatronics*, vol. 24, no. 1, pp. 36–44, 2019.

[52] C. Cao, T. L. Hill, and A. T. Conn, "On the nonlinear dynamics of a circular dielectric elastomer oscillator," *Smart Mater. Struct.*, vol. 28, no. 7, p. 075020, 2019.

[53] C. Cao, X. Gao, and A. T. Conn, "Towards efficient elastic actuation in bio-inspired robotics using dielectric elastomer artificial muscles," *Smart Mater. Struct.*, 2019.

[54] J.-S. Plante, "Dielectric Elastomer Actuators for Binary Robotics and Mechatronics," *IEEE/ASME Trans. Mechatronics*, vol. 17, no. 5, p. 186, 2006.

[55] T. Li, Z. Zou, G. Mao, and S. Qu, "Electromechanical Bistable Behavior of a Novel Dielectric Elastomer Actuator," *J. Appl. Mech.*, vol. 81, no. 4, p. 041019, 2013.

[56] M. Hodgins, A. York, and S. Seelecke, "Experimental comparison of bias elements for out-of-plane DEAP actuator system," *Smart Mater. Struct.*, vol. 22, no. 9, p. 094016, 2013.

[57] M. Follador, M. Cianchetti, and B. Mazzolai, "Design of a compact bistable mechanism based on dielectric elastomer actuators," *Meccanica*, vol. 50, no. 11, pp. 2741–2749, 2015.

[58] N. Wang, C. Cui, B. Chen, H. Guo, and X. Zhang, "Design of Translational and Rotational Bistable Actuators Based on Dielectric Elastomer," *J. Mech. Robot.*, vol. 11, no. 4, p. 041011, 2019.

[59] C. T. Nguyen, H. Phung, T. D. Nguyen, H. Jung, and H. R. Choi, "Multiple-degrees-of-freedom dielectric elastomer actuators for soft printable hexapod robot," *Sensors Actuators, A Phys.*, vol. 267, pp. 505–516, 2017.

[60] G. Berselli, R. Vertechy, G. Vassura, and V. Parenti-Castelli, "Optimal synthesis of conically shaped dielectric elastomer linear actuators: Design methodology and experimental validation," *IEEE/ASME Trans. Mechatronics*, vol. 16, no. 1, pp. 67–79, 2011.

[61] B. Xu, R. Mueller, A. Theis, M. Klassen, and D. Gross, "Dynamic analysis of dielectric elastomer actuators," *Appl. Phys. Lett.*, vol. 100, no. 11, p. 112903, 2012.

[62] F. Wang, T. Lu, and T. J. Wang, "Nonlinear vibration of dielectric elastomer incorporating strain stiffening," *Int. J. Solids Struct.*, vol. 87, pp. 70–80, 2016.

[63] J. Zhang, H. Chen, and D. Li, "Modeling nonlinear dynamic properties of dielectric elastomers with various crosslinks, entanglements, and finite deformations," *J. Appl. Phys.*, vol. 123, no. 8, p. 084901, 2018.

[64] A. Alibakhshi and H. Heidari, "Analytical approximation solutions of a dielectric elastomer balloon using the multiple scales method," *Eur. J. Mech. A/Solids*, vol. 74, no. October 2018, pp. 485–496, 2019.

[65] H. Vatanjou, Y. Hojjat, and M. Karafi, "Nonlinear dynamic analysis of dielectric elastomer minimum energy structures," *Appl. Phys. A*, vol. 125, no. 9, p. 583, 2019.

[66] C. Chiang Foo, S. Cai, S. Jin Adrian Koh, S. Bauer, and Z. Suo, "Model of dissipative dielectric elastomers," *J. Appl. Phys.*, vol. 111, no. 3, p. 034102, 2012.

[67] A. . Gent, "A New Constitutive Relation for Rubber," *Rubber Chem. Technol.*, vol. 69, no. 1, pp. 59–61, 1996.

[68] J. Sheng, H. Chen, B. Li, and Y. Wang, “Nonlinear dynamic characteristics of a dielectric elastomer membrane undergoing in-plane deformation,” *Smart Mater. Struct.*, vol. 23, no. 4, p. 045010, 2014.

[69] S. Rosset, O. A. Araromi, J. Shintake, and H. R. Shea, “Model and design of dielectric elastomer minimum energy structures,” *Smart Mater. Struct.*, vol. 23, no. 8, p. 085021, 2014.

[70] S. Michel, X. Q. Zhang, M. Wissler, C. Löwe, and G. Kovacs, “A comparison between silicone and acrylic elastomers as dielectric materials in electroactive polymer actuators,” *Polym. Int.*, vol. 59, no. 3, pp. 391–399, 2010.

[71] D. Wagg and S. Neild, *Nonlinear vibration with control*. Dordrecht, 2009.

[72] Y. Li, I. Oh, J. Chen, H. Zhang, and Y. Hu, “Nonlinear dynamic analysis and active control of visco-hyperelastic dielectric elastomer membrane,” *Int. J. Solids Struct.*, vol. 152–153, pp. 28–38, 2018.

[73] H. Dankowicz and F. Schilder, *Recipes for Continuation*. Society for Industrial & Applied Mathematics, U.S., 2013.

**Figures**

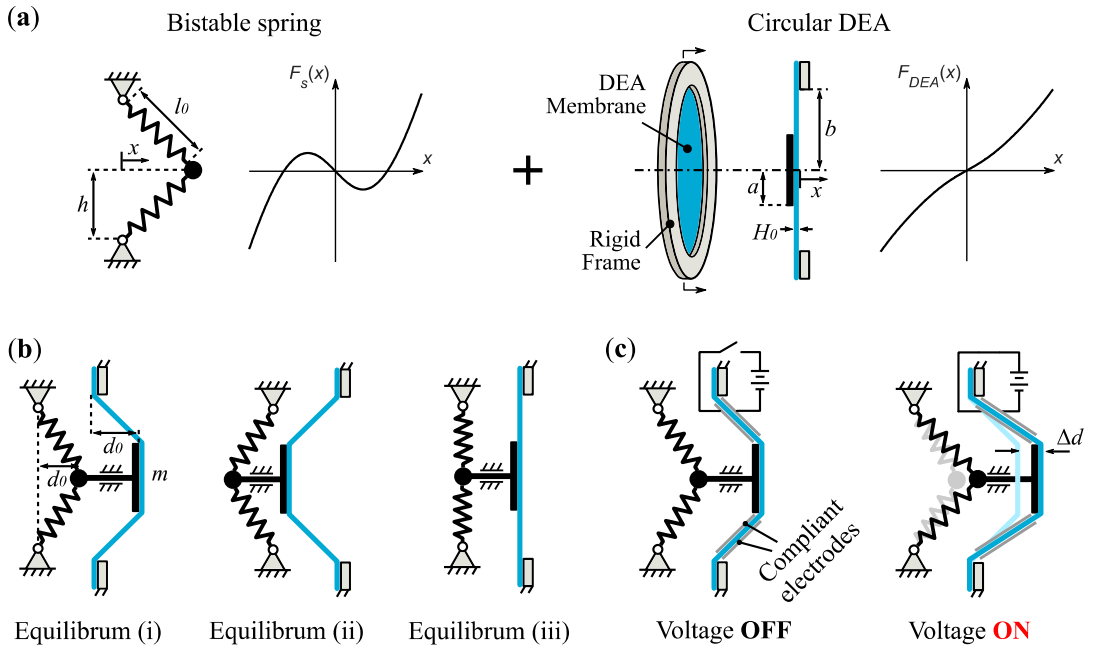


**Figure 1**. Design concept and working principle of the DEO. (**a**) The DEO consists of a bistable mechanism and a circular DEA. (**b**) Three possible static equilibrium states of the DEO. (**c**) Quasi-static actuation principle of the DEO.

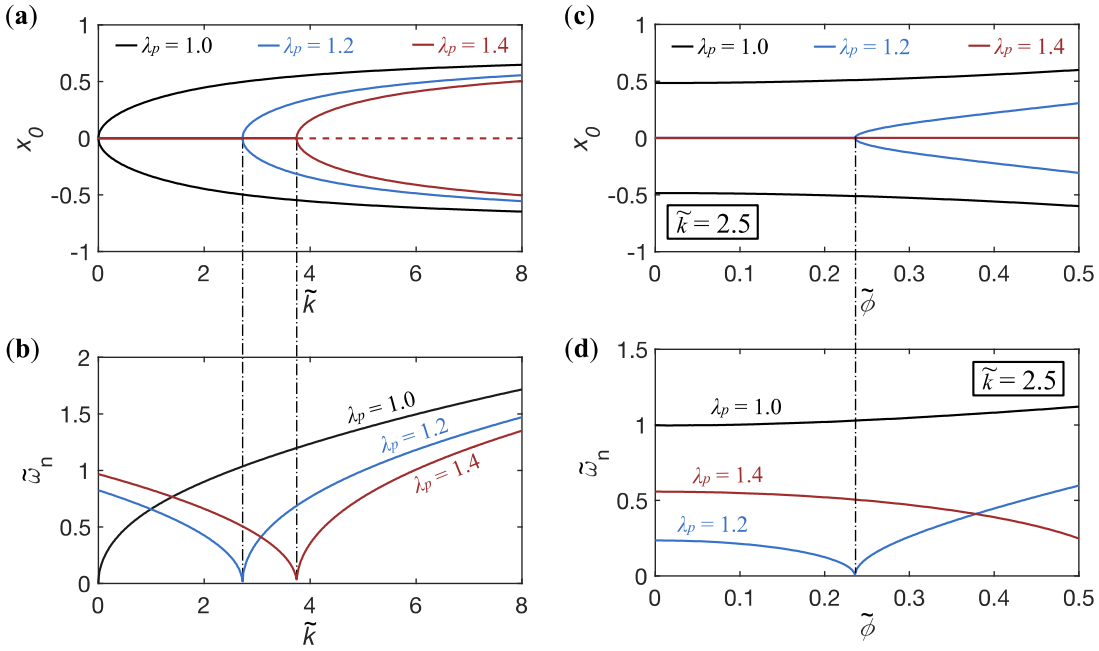


**Figure 2**. (**a**) Equilibrium points of the DEO and (**b**) the natural frequency as a function of non-dimensional stiffness $\tilde{k}$ with the pre-stretch ratio of 1.0, 1.2 and 1.4. Stable solutions are plotted with solid lines in (**a**) while the unstable ones are represented by a dashed line. (**c**) Equilibrium points of the DEO and (**d**) the natural frequency as a function of non-dimensional biasing voltage $\tilde{\phi}$ with the pre-stretch ratio of 1.0, 1.2 and 1.4.

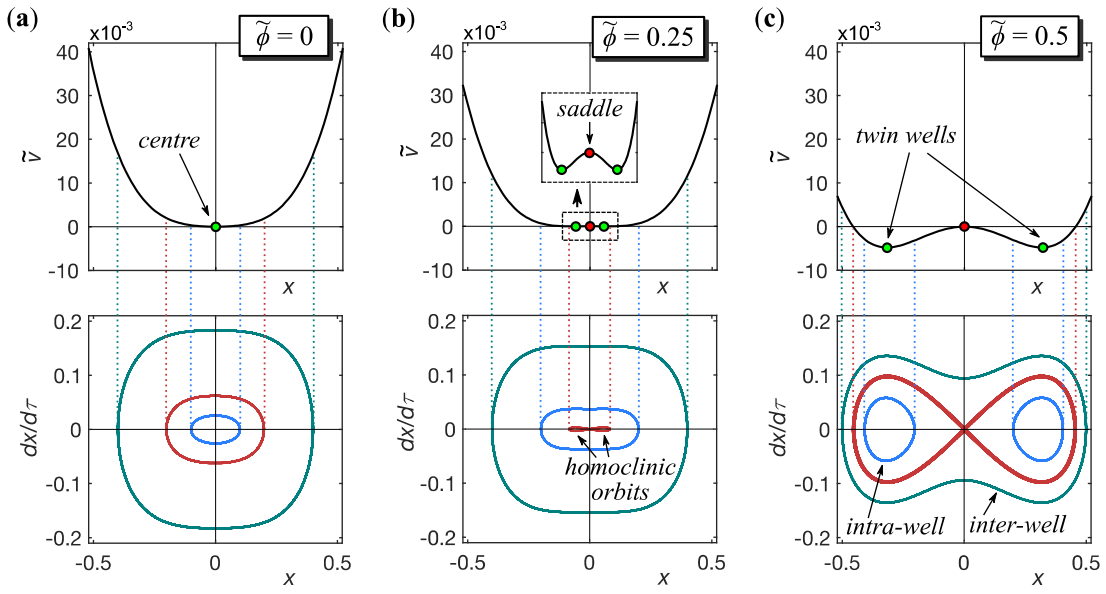


**Figure 3**. The potential energy function of the system and the phase portraits for (**a**) $\tilde{\phi} = 0$, (**b**) $\tilde{\phi} = 0.25$ and (**c**) $\tilde{\phi} = 0.5$. Thick red curves in the phase portraits in (**b**) and (**c**) denote the homoclinic orbits.

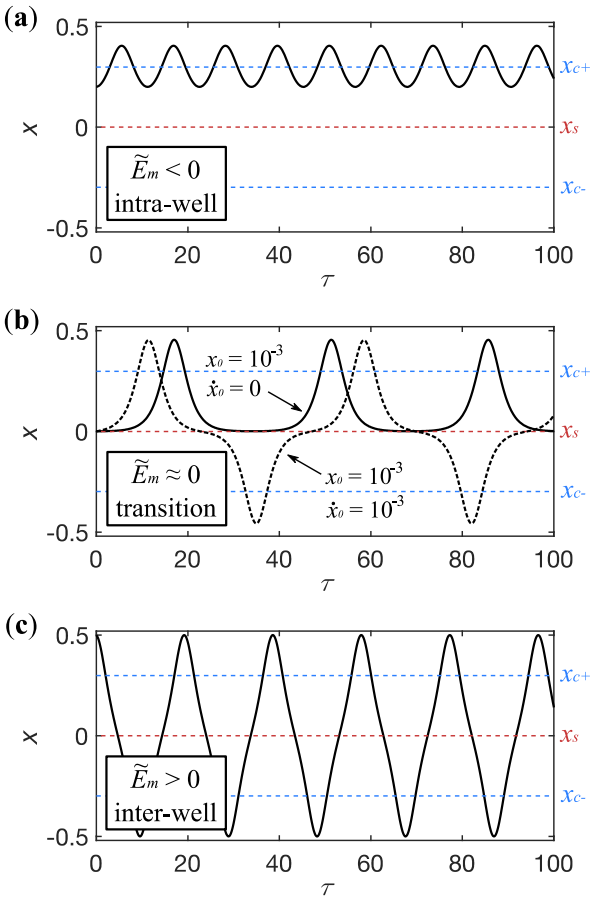


**Figure 4**. Time series of the free oscillation with total mechanical energy (**a**) $\tilde{E}_m < 0$, the response oscillates intra-well; (**b**) $\tilde{E}_m \cong 0$, the response transits from intra- ($\tilde{E}_m < 0$) to inter-well ($\tilde{E}_m > 0$) and; (**c**) $\tilde{E}_m > 0$, the system undergoes high amplitude inter-well oscillation. The DC voltage is $\tilde{\phi} = 0.5$ in all cases.

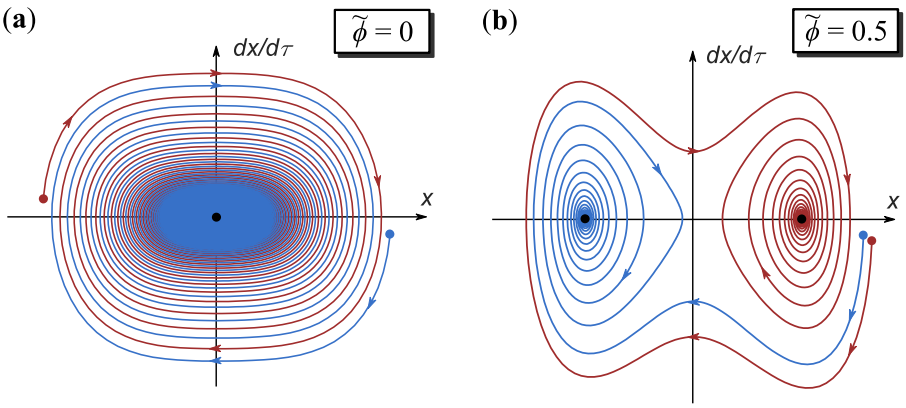


**Figure 5**. Examples of nonconservative phase portraits. (**a**) $\tilde{\phi} = 0$, the DEO system has a single attractor in the origin. (**b**) $\tilde{\phi} = 0.5$, the DEO system has two symmetrical attractors at $x$ = -0.31 and $x$ = 0.31. Two points with close initial conditions are attracted to two different equilibrium points. $\tilde{c} = 0.5$.

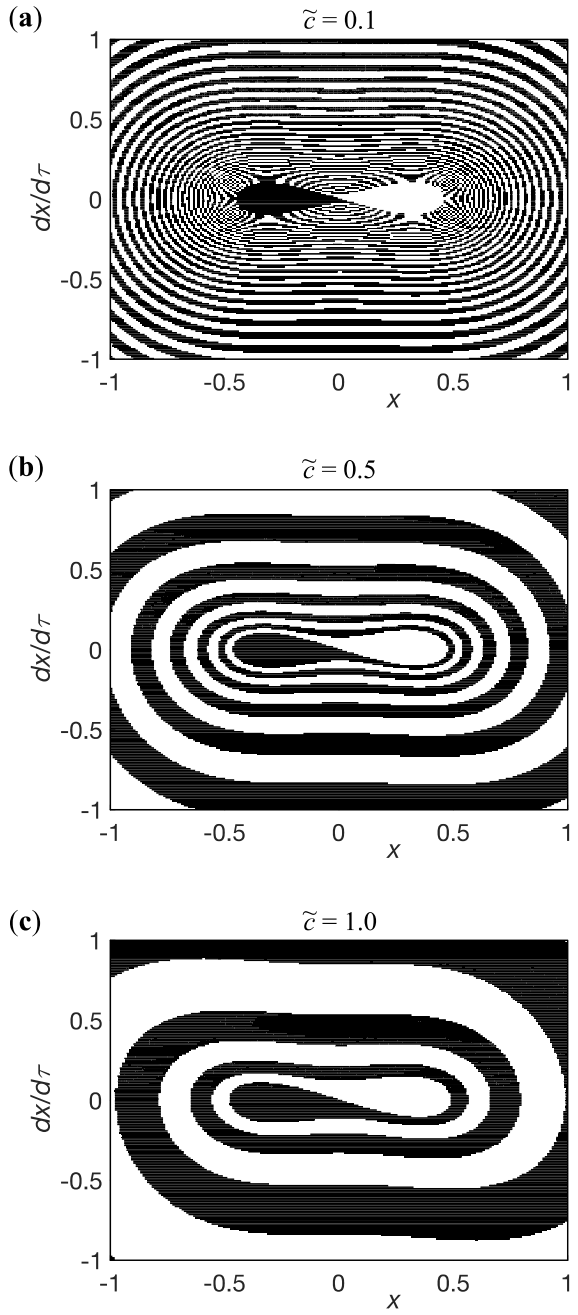


**Figure 6**. Basins of attraction for the DEO system with (**a**) $\tilde{c} = 0.1$, (**b**) $\tilde{c} = 0.5$ and, (**c**) $\tilde{c} = 1.0$. The black and white regions indicate a landing on the equilibrium point of $x$ = -0.31 and $x$ = 0.31 respectively.

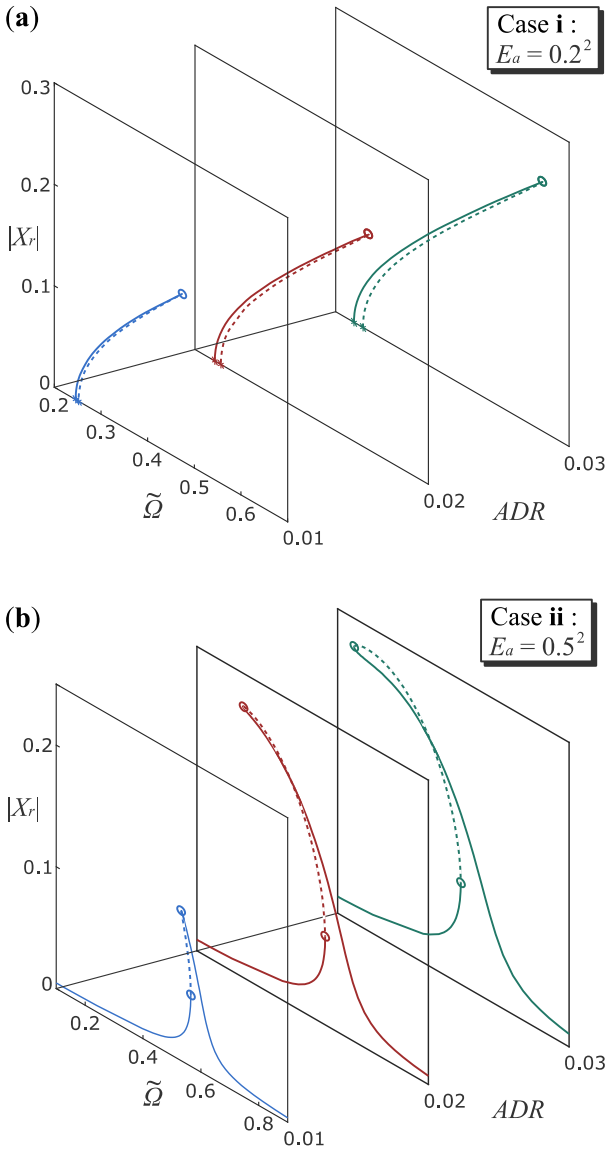


**Figure 7**. Frequency response of the DEO system under low *ADR* ratio parametric excitation with (**a**) case **i**: $E_a = 0.2^2$ and (**b**) case **ii**: $E_a = 0.5^2$. Circular markers indicate fold bifurcations and dashed curves represent unstable solutions.

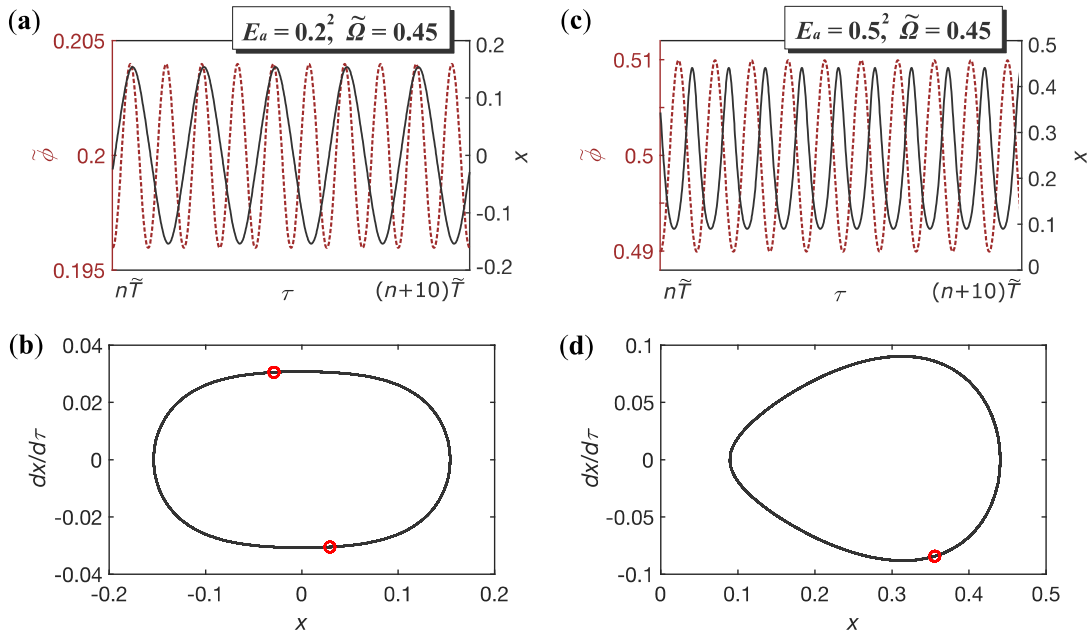


**Figure 8**. Examples of the steady state response of the DEO system under parametric excitation with $ADR$ = 0.02. (**a**) Time series and (**b**) phase portrait and Poincaré map for the steady-state response at $\widetilde{\Omega} = 0.45$ and $E_a = 0.2^2$. (**c**) Time series and (**d**) phase portrait and Poincaré map for the steady-state response at $\widetilde{\Omega} = 0.45$ and $E_a = 0.5^2$.

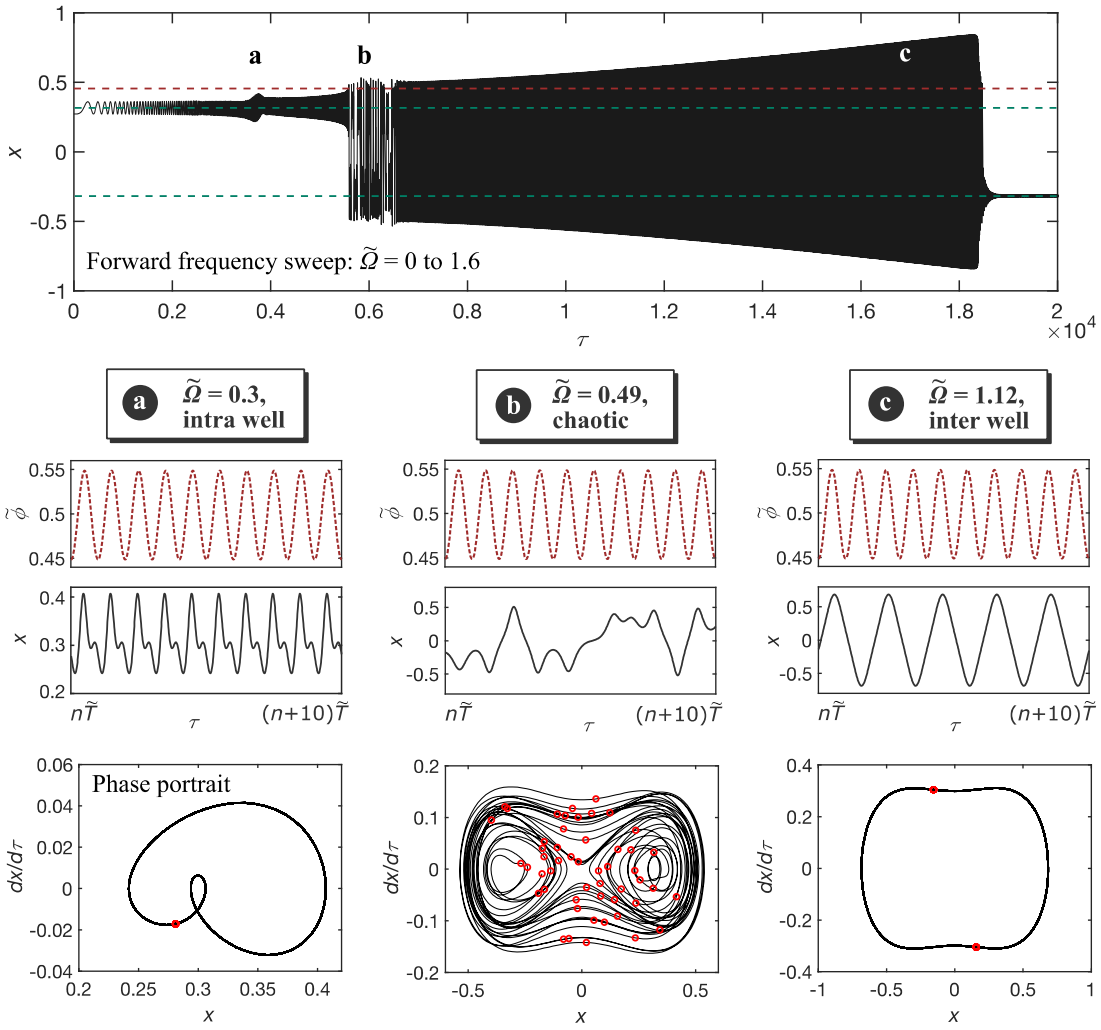


**Figure 9**. Frequency sweep of the DEO system showing the transition from low amplitude intra-well oscillation to high amplitude inter-well oscillations. A chaotic response is found during the transition.

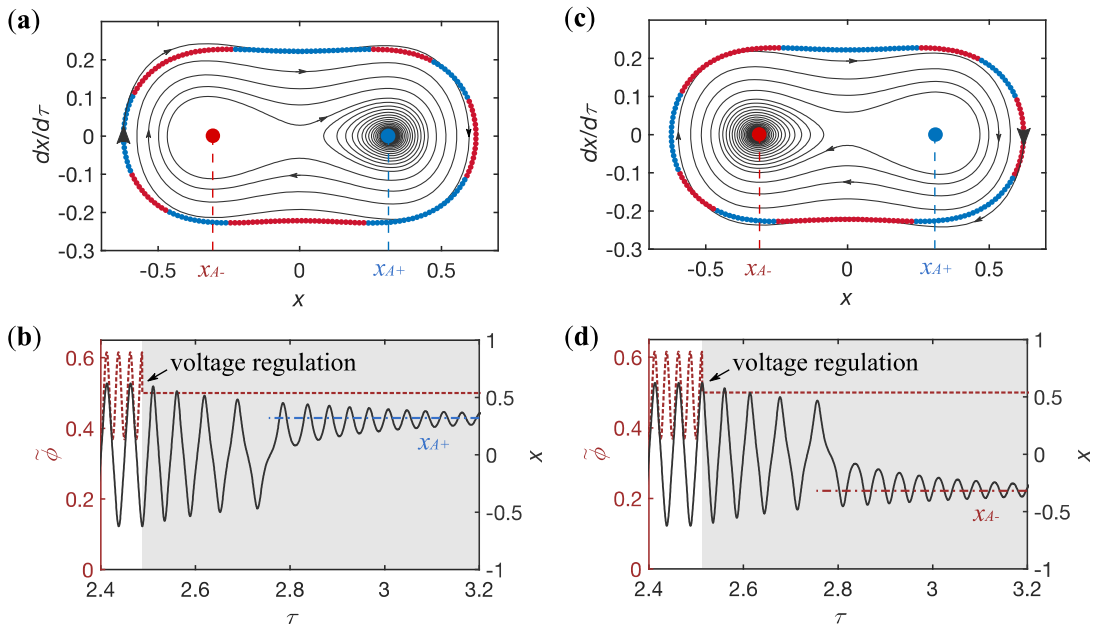


**Figure 10**. Attractor map for a steady periodic response of the DEO system at $ADR = 0.25$ and $\tilde{\Omega} = 0.9$ and oscillation control examples using the attractors map. (**a**) Phase portraits of the controlled targeting equilibrium $x_{A+}$. (**b**) Time histories of the example in (**a**), the actuation voltage is regulated when the states satisfy the desired initial conditions. (**c**) Phase portraits and (**d**) time histories control targeting the initial conditions in red landing to the equilibrium $x_{A-}$.

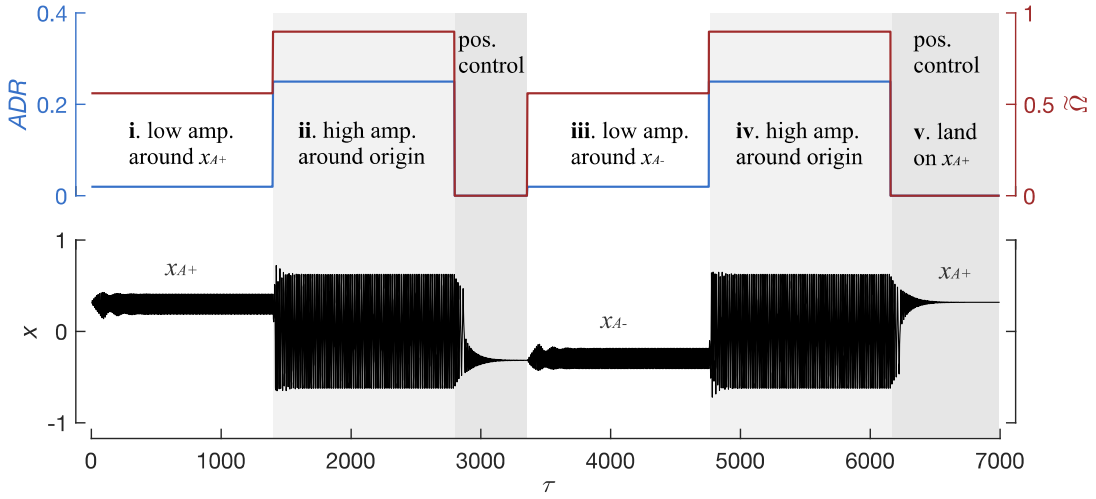


**Figure 11**. Examples showing the DEO system can be actively controlled to oscillate around the desired equilibrium points.